19

An Asymmetric Magneto-Optical Trap

Heung-Ryoul Noh[1] and Wonho Jhe[2]
Chonnam National University
Seoul National University
Korea

1. Introduction

Since the advent of the magneto-optical trap (MOT) in 1987 (Raab et al., 1987), it has been intensively studied and widely used as a pre-cooled atomic source for various experiments (Metcalf & van der Straten, 1999). In addition, there have been intensive studies on the MOT itself such as cold collisions (Walker & Feng, 1994), nonlinear optics (Tabosa et al., 1991), existence of sub-Doppler force (Wallace et al., 1994), or limit of density (Townsend et al., 1995). Nevertheless MOT itself is far from quantitative understanding and still keeps providing surprises as unexplored characteristics and applications are being developed. In the perspective of nonlinear dynamics in a MOT, there were several reports as follows: Sesko *et al*. observed several variations of atomic spatial distribution and abrupt change between the distributions when there exist laser beam misalignment, intensity imbalance or radiation trapping (Walker et al., 1990; Sesko et al., 1991). They explained the phenomena by optical torques exerted by the misaligned trapping lasers. Based on the studies of Sesko *et al.*, Bagnato *et al.* have observed the limit cycles and some abrupt changes of atomic spatial distributions (Bagnato et al., 1993; Dias Nunes et al., 1996). Recently, Wilkowski *et al.* found the instability phenomena in a MOT and explained them by means of shadow effect (Wilkowski et al., 2000; di Stefano et al, 2003). In addition, MOT exhibits very unique collective effects and critical behaviors when the number of atoms increases such as instability-induced pulsation (Labeyrie et al., 2006), and plasma oscillations of ultracold neutral plasma (Kulin et al., 2000).

In this article we present experimental and theoretical works on the applications of the magneto-optical trap by modifying the trap conditions, which is termed as an asymmetric magneto-optical trap (AMOT). This article is composed of three parts: In Sec. 2, we describe the parametric resonance achieved by the modulation of the trap laser intensities. When the modulation frequency is near twice the natural frequency of the trap and the modulation amplitude exceeds a threshold value, the parametric resonance can be excited; i.e., the trapped atoms are divided into two parts and oscillate in opposite directions. The various theoretical and experimental studies are presented. Section 3 is devoted to measurement of trap parameters by the method of parametric resonance and transient oscillation. By decreasing the modulation amplitude of the parametric excitation down to its threshold value one can measure the trap frequency. In the case of transient oscillation, the trap frequency and damping coefficient were obtained by measuring the trajectory of the atoms returning to the original trap center, after the applied uniform magnetic field, used for

Source: Recent Optical and Photonic Technologies, Book edited by: Ki Young Kim,
ISBN 978-953-7619-71-8, pp. 450, January 2010, INTECH, Croatia, downloaded from SCIYO.COM

displacing the trap center, was turned off. In Sec. 4, we discusses adjustable trap where the trap-laser frequencies are unequal to one another. When the detuning of the laser along the symmetric axis is different from those of the transverse lasers, an array of several sub-Doppler traps with adjustable separations between the traps which are proportional to the relative laser-detuning difference.

2. Parametric resonance in a magneto-optical trap

The parametric resonances are ubiquitous phenomena: e.g., we can find them in vertically driven pendulum, fluid mechanics, ion trap such as a Paul trap or a Penning trap, optical dipole trap, and a lot of different fields (Landau & Lifshitz, 1976; Nayfeh & Moore, 1979). In an optical lattice or a dipole trap, the modulation of the potential depth was often used to measure the vibrational frequencies (Friebel et al., 1998). In a Paul trap, the observation of higher order resonance up to n = 10 has been reported (Razvi et al., 1998). Above all, our study is very analogous to parametrically-pumped electron oscillators in the Penning trap (Tan & Gabrielse, 1991; 1993; Tseng et al., 1999; Lapidus et al., 1999). The simple observed features of electrons in the cylindrical Penning trap are related to the cooperative behavior and nonlinear dynamics. The electron oscillators exhibit a rich and varied nonlinear dynamics which our systems also manifested.

In this section, we present the theoretical and experimental results of the parametrically driven MOT by using the modulation of the MOT potential, especially the cooling laser intensity (Kim et al., 2003; 2004). When we modulate the intensity of the cooling laser at about twice the resonant frequency of the trap, the atoms in the MOT are divided into two parts and oscillate reciprocally with the finite amplitude due to nonlinearity of the trap. The amplitude of oscillation and the phase with respect to the modulation of cooling laser are measured with the images of atomic cloud and compared to the theoretical calculations. Direct observation of the sub-Doppler trap in the parametrically driven MOT is also described (Kim et al., 2004).

2.1 Theory

The atomic motion in a parametrically-driven MOT can be described in terms of simple Doppler cooling theory. In the MOT the $\sigma^+(\sigma^-)$ polarized light propagates from the $-z(+z)$ axis, while the $\sigma^-(\sigma^+)$ polarized light propagates from the $-x(+x)$ and $-y(+y)$ axis. Also the inhomogeneous magnetic field is applied, which is given by

$$\vec{B} = b\left(-\frac{x}{2}\hat{x} - \frac{y}{2}\hat{y} + z\hat{z}\right),$$

where b is the magnetic field gradient for z-axis. The laser intensities are modulated to excite the parametric resonance. Although intensities of all laser beams are simultaneously modulated with the frequency ω, we can excite the resonance for one specific axis by controlling the parameters such as laser intensity or the detuning. In this study we only excite the parametric resonance for z-axis.

The atomic motion for z-axis can be described by the following equation for a two-level atom (Metcalf & van der Straten, 1999),

$$m\ddot{z} = F(z, \dot{z}, t), \tag{1}$$

with

$$F(z,\dot{z},t)=\frac{\hbar k\Gamma}{2}\left[\frac{s_0(1+h\cos\omega t)}{1+s_0(1+h\cos\omega t)+4(\delta-k\dot{z}-\frac{\mu_B b}{\hbar}z)^2/\Gamma^2}\right.$$

$$\left.-\frac{s_0(1+h\cos\omega t)}{1+s_0(1+h\cos\omega t)+4(\delta+k\dot{z}+\frac{\mu_B b}{\hbar}z)^2/\Gamma^2}\right], \tag{2}$$

where k is the wave vector, μ_B is Bohr magneton, m is the mass of an atom, Γ is the decay rate of the excited state (=$2\pi\times$5.9 MHz), and δ(= ω_L – ω_A) is the detuning of the laser frequency ω_L relative to the atomic resonance frequency ω_A. Here s_0(= I/I_s) is the unmodulated saturation parameters with I being the laser intensity of a laser beam for z-axis and I_s (=1.62 mW/cm^2) being the saturation intensity for a ^{85}Rb atom, and the term (1+$h$cosωt) describes the modulated laser intensity, where h is the modulation amplitude and ω is the modulation frequency.

In addition to the Doppler force in Eq. (2), we need to include the sub-Doppler force and the random force (Chang & Minogin, 2002). The sub-Doppler force describes the tight confinement in the vicinity of the origin of velocity or position and explains the bright and small trap at the origin. In the former part of Sec. 2, we ignore this force, since we do not consider the small trap and describes the motion with large amplitude. The random force which stems from the recoil of the emitted photon from atoms contributes to the determination of the width of trap and the transitions between the stable attractors. As far as the center of motion is concerned, however, we do not need to include this force. When we discuss the simulations about the width of oscillating clouds, we will include this force.

We present analytic solutions from the approximation of Eq. (1) in order to have concrete understanding of the system. When we expand the Eq. (1) up to third orders in position (z) and velocity ($\dot{z}$), Eq. (1) can be approximately written by

$$\ddot{z}+\beta\dot{z}+\omega_0^2(1+h\cos\omega t)z=-A_0\omega_0^2\left[z+\frac{\beta}{\omega_0^2}\dot{z}\right]^3, \tag{3}$$

where the natural frequency (ω_0), the damping coefficient (β), and the nonlinear coefficient (A_0) are given by

$$\omega_0=\sqrt{\frac{8k\mu_B b s_0(-\delta/\Gamma)}{m\left[1+4(\delta/\Gamma)^2\right]^2}}, \tag{4a}$$

$$\beta=\frac{\hbar k}{\mu_B b}\omega_0^2, \tag{4b}$$

$$A_0=8\left(\frac{\mu_B b}{\hbar\Gamma}\right)^2\frac{4(\delta/\Gamma)^2-1}{\left[4(\delta/\Gamma)^2+1\right]^2}, \tag{4c}$$

respectively. Here we have assumed that $h \ll 1$ and the damping is weak, that is, $\beta \ll \omega_0$. When we neglect the nonlinear term in Eq. (3), i.e., the term in the right hand side of Eq. (3), it becomes

$$\ddot{z} + \beta\dot{z} + \omega_0^2(1 + h\cos\omega t)z = 0, \tag{5}$$

which is a well-known Mathieu equation (Landau & Lifshitz, 1976; Nayfeh & Moore, 1979). The solutions of Mathieu equation exhibit the parametric resonance which occurs when the modulation frequency is $\omega = 2\omega_0/n$, where n is the integers. In practice, it is hardly possible to observe higher order resonances ($n > 1$). In the absence of damping of the system ($\beta = 0$), the parametric resonance occurs in the range

$$-\frac{1}{2}h\omega_0 < \omega - 2\omega_0 < \frac{1}{2}h\omega_0, \tag{6}$$

which is expressed as dotted lines in Fig. 1(a). Here the horizontal axis is the modulation amplitude (h), and the vertical axis is the modulation frequency normalized to the trap frequency (ω/ω_0). When the modulation frequency lies inside this region, the solution diverges and shows instability. If we take into account the damping, the parametric resonance range slightly changes from Eq. (6) to $\omega_1 < \omega < \omega_2$ as shown in Fig. 1(a) (solid curve), where the characteristic frequencies, ω_1 and ω_2, are given by

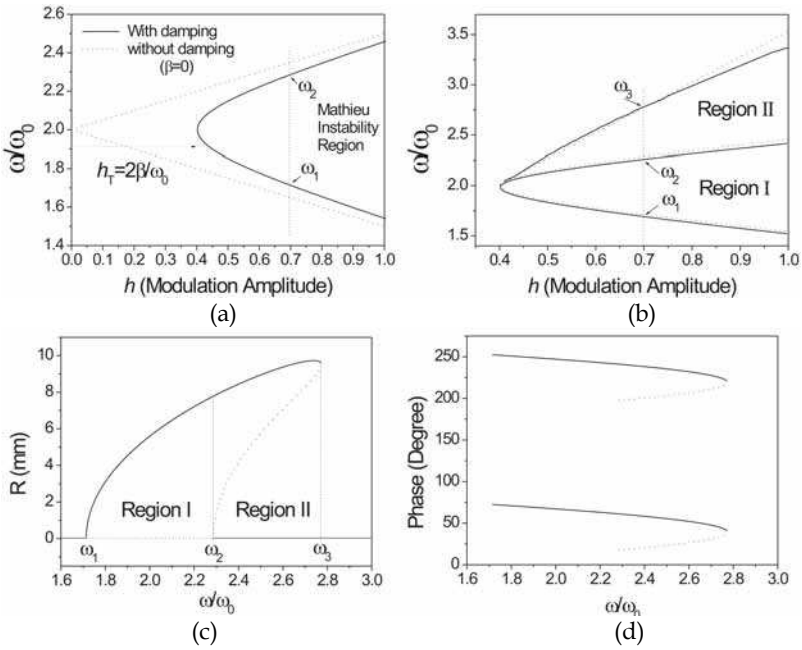

Fig. 1. (a) The instability region of the parametrically driven MOT. (b) The numerically calculated map from Eq. (1) as solid curves, while the result with the linearized Mathieu equation is plotted as a dotted line or curves. The calculated amplitude R (c) and the phase ψ (d) of the limit cycle at the modulation amplitude of $h = 0.7$.

$$\omega_{1(2)} = 2\omega_0 - (+)\frac{\omega_0}{2}\sqrt{h^2 - h_T^2}. \tag{7}$$

Here a threshold value (h_T) of the modulation amplitude above which the parametric resonance can occur is given by $h_T = 2\beta/\omega_0$.
Including the nonlinear terms, Eq. (3) can be analytically solved by means of usual averaging method (Nayfeh & Moore, 1979; Strogatz, 2001). In this case, the stability map is changed (Fig. 1(b)). In the steady-state regime in the rotating frame with the angular frequency $\omega/2$, the nontrivial solutions of Eq. (3) can be written by

$$z(t) = R(t)\cos\left[\frac{\omega}{2}t + \psi(t)\right], \tag{8}$$

where the amplitude $R(t)$ and the phase $\psi(t)$ satisfy the following equations:

$$\frac{dR}{dt} = -\frac{\beta}{2}R\left[1 + \frac{3}{16}(4 + h_T^2)A_0R^2 - \frac{h}{h_T}\sin 2\psi\right],$$

$$\frac{d\psi}{dt} = -\frac{\omega - 2\omega_0}{2} + \frac{h\omega_0}{4}\cos 2\psi + \frac{3}{32}(4 + h_T^2)A_0\omega_0R^2. \tag{9}$$

The solution in Eq. (8) is called a limit cycle motion, which comes from the reduction of the divergent solution to the finite one owing to the nonlinear term in Eq. (3).
The steady state solutions can be obtained by equating $dR/dt = 0$ and $d\psi/dt = 0$ in Eq. (9). We immediately notice that there exists a trivial solution $R = 0$. As well, we have the nontrivial steady-state solutions for Eq. (9) as

$$R^2 = \frac{16}{3A_0(4 + h_T^2)^2}\left(4(\eta - 2) - h_T^2 \pm \sqrt{h^2(4 + h_T^2) - 4h_T^2(\eta - 1)^2}\ \right),$$

$$\cos 2\psi = \frac{2}{h(4 + h_T^2)^2}\left(h_T^2(\eta - 1) \mp \sqrt{h^2(4 + h_T^2) - 4h_T^2(\eta - 1)^2}\ \right), \tag{10}$$

where the upper (lower) sign denotes the stable (unstable) solutions and $\eta(= \omega/\omega_0)$ is the normalized modulation frequency. The calculated results for the amplitude and phase are shown in Fig. 1(c) and 1(d), respectively, for $h = 0.7$. In Figs. 1(c) and 1(d), the stable (unstable) solutions are represented as solid (dotted) lines. We can see that there exist three characteristic frequencies (ω_1, ω_2 and ω_3) which characterize the existence of solutions. The frequencies ω_1 and ω_2 are already defined in Eq. (7) and the new frequency ω_3 is given by

$$\omega_3 = \omega_0\left(1 + \frac{h}{2h_T}\sqrt{4 + h_T^2}\right). \tag{11}$$

The frequency ω_3 does not exist for solutions of the Mathieu equation and arises when the nonlinear term is included. As shown in Fig. 1(b) (dotted line), the frequency ω_3 is linearly dependent on the modulation amplitude h.

In Figs. 1(c) and 1(d), for the frequency range $\omega_1 < \omega < \omega_2$ (Region I), as well as an unstable solution ($R = 0$), there exist two stable solutions. This is because for a given amplitude R, we have two solutions of the phase with the difference of 180° (Fig. 1(d)). When the nonlinear terms are neglected, the solution in this region exhibits instability. Due to the nonlinear terms, however, the solution ceases to diverge and have a finite value, which is called a limit cycle. When the frequency lies at the range $\omega_2 < \omega < \omega_3$ (Region II), we have three stable (solid line and curves) and two unstable solutions (dotted curves). Of three stable solutions, one is a stable attractor at the origin ($R = 0$) and the others are limit cycles with phase difference of 180°. In the other frequency region ($\omega < \omega_1$ or $\omega > \omega_3$), there exists one stable attractor at the origin. As can be seen in the experiment, while a limit cycle motion is presented as oscillating clouds with the frequency of $\omega/2$, the stable attractor at the origin is represented by a stationary trap.

When the modulation frequency increases, a trivial solution (stable attractor at the origin) converts to the limit cycle motion at the frequency $\omega = \omega_1$, which is called a super-critical Hopf bifurcation (Strogatz, 2001). In contrast, when the frequency decreases from the larger frequency region, the combination of a stable attractor at the origin and the limit cycle motions changes to the limit cycle motions alone at the frequency $\omega = \omega_2$, which is called a sub-critical Hopf bifurcation (Strogatz, 2001). In general we observe the hysteresis: when we increase the frequency across the frequency ω_2 we follow the nontrivial solution at Region II in Fig. 1(c). On the contrary, when we sweep down the frequency crossing the frequency ω_3, the solution is merely a trivial solution ($R = 0$). In reality, however, it is not possible to observe this normal hysteresis effect, which will be explained later. Comparison of numerical calculations of Eq. (1) with the results with the analytic solutions are shown in Fig. 1(b). In Fig. 1(b), the dotted curve denotes the results of Fig. 1(a). That is, they were obtained for the linearized Mathieu equation (Eq. (5)). Also the solid curve is the result of the numerical calculation. We can notice that ω_1 and ω_2 are slightly shifted towards smaller values.

The atomic motion can be described more clearly in the rotating frame with the angular velocity of $\omega/2$. In that frame, Eq. (9) can be transformed to the following equations:

$$\frac{dq_1}{dt} = -\frac{\beta}{2} q_1 \left(1 + q^2\right) + \frac{\omega_0}{2} q_2 \left(\frac{h}{2} + \Omega - q^2\right),$$

$$\frac{dq_2}{dt} = -\frac{\beta}{2} q_2 \left(1 + q^2\right) + \frac{\omega_0}{2} q_1 \left(\frac{h}{2} - \Omega + q^2\right), \tag{12}$$

where the dimensionless amplitudes are defined by $q_1 = q\cos\psi$ and $q_2 = q\sin\psi$, with

$$q^2 = q_1^2 + q_2^2 = \frac{3}{16}(4 + h_r^2) A_0 R^2, \quad \Omega = \frac{\omega - 2\omega_0}{\omega_0}.$$

The calculated stability regions in the rotating frame are plotted in Fig. 2(a) for $\omega/\omega_0 = 2.0$ (Region I in Fig. 1(c)) and Fig. 2(b) for $\omega/\omega_0 = 2.5$ (Region II in Fig. 1(c)). In Fig. 2 the stable (unstable) points are denoted by the filled circles (triangles). In Fig. 2(a), there are two stability regions, which are divided by two spiral-shaped regions. We have two stable points inside the regions and one unstable point at the border of two regions. An atom with initial condition in one specific region converges to a stable point which belongs to that region. In

Fig. 2(b), there exist three stable points and two unstable points. The regions are divided by three spiral-shaped regions. The behaviors of atomic motions are analogous to those in Fig. 2(a).

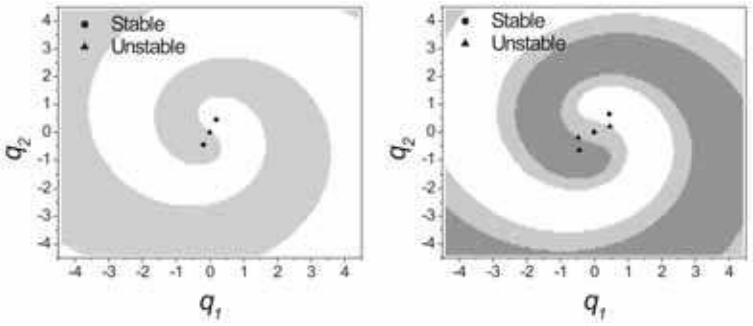

(a) (b)

Fig. 2. The stability regions for the frequency Region I (a) and Region II (b).

When the modulation frequency corresponds to Region II in Fig. 1(b) or Fig. 1(c), in the experiment, the initial conditions of trapped atoms reside in the central spiral-shaped region in Fig. 2(a). Thus we only observe a stationary trap when the frequency is swept down across ω_3. On the contrary, when we sweep up the frequency crossing ω_2, we only observe the two limit cycle motions, because the initial conditions reside in the two large spirals. That is to say, we may observe hysteresis. However, in Region II, as will be seen in the next subsection, we can always observe the limit cycle motions as well as the central trap independent of the direction of the frequency sweeping. There are two reasons for the disappearance of the hysteresis effect. The first one is the fact that the atoms are always loaded from background atoms and lost due to the collisions with them. Thus the initial conditions cover the broad regions including three spiral-shaped regions. As a result, both the central trap and the limit cycle motions can be observed simultaneously in the experiment. The second reason is the existence of the diffusion. In the experiment there always exists diffusion which provokes atoms to make transition from the fixed point to the limit cycle motions. Therefore, although the frequency is swept downwards crossing ω_3, we can observe the limit cycles as well as the stationary trap. In reality, both reasons exist simultaneously, and contribute to the disappearance of the hysteresis effect.

2.2 Experimental and simulation results

We study parametric resonance of atoms in a standard vapor-cell MOT where the intensity of cooling laser is modulated. We used the first order diffracted laser beam by an acousto-optic modulator (AOM), which can vary the laser power in accordance with the applied voltage. The ^{85}Rb atoms in the MOT have three dimensional confinements with the natural frequency ω_0 ($\omega_0/\sqrt{2}$) for z (x or y)-axis, where ω_0 is defined in Eq. (4a). In order to observe the parametric resonance and limit cycle motion in the MOT, the s_0 should be very small (< 0.1). In the experiment we excite parametric resonance for z-axis (the axis of anti-Helmholtz coils). For z-axis, $s_0 = 0.042$ (or 0.05), $b = 9$ G/cm, $\delta = -2.9\ \Gamma$, and $h = 0.9$ (or 0.7). Accordingly, $\omega_0 = 2\pi \times 31.5(34.3)$ s^{-1} and $h_T = 0.40$ (or 0.44). Thus the modulation amplitude should be

greater than 0.40 (0.44) to excite parametric resonance, even if the modulation frequency is exactly twice the resonance frequency. On the other hand, the normalized laser intensity for x- or y-axis is about $5s_0$. Accordingly the corresponding threshold modulation amplitude is 0.9, which is not smaller than the modulation amplitude in the experiment. This is why only in the z-axis there occurs parametric resonance, although the cooling laser intensities for all three directions are modulated at the same frequency and modulation amplitude.

When the intensity of the cooling laser is modulated at about twice of its natural frequency, the atoms are divided into two parts and oscillate in opposite directions with the finite amplitudes. The typical photos of oscillating atomic clouds are shown in Fig. 3. The images of the cloud are taken at every 1 ms for 1/2400 s of exposure time. Here s_0 = 0.042, and the modulation frequency is 75 Hz (ω/ω_0= 2.38) for (a) and 95 Hz (ω/ω_0= 3.02) for (b). In all cases the modulation amplitude is 0.9. The modulation frequencies for the results in Figs. 3(a) and 3(b) belong to Region I and Region II in Fig. 1(b) or Fig. 1(c), respectively. As explained in the previous subsection, we have two stable points (limit cycles) in Region I (Fig. 3(a)) and three stable points (one fixed point and two limit cycles) in Region II (Fig. 3(b)). The bright spot in Fig. 3(b) is due to this sub-Doppler force (see Sec. 2.3). Figure 4 shows the series of signals measured for Region I (a) and Region II (b). The whole period is $2\pi/\omega$, which is the period of modulation signal and half the period of atomic oscillations, and the signals are equally separated in time. We can clearly see that the atomic clouds are divided into two parts and oscillate in opposite directions.

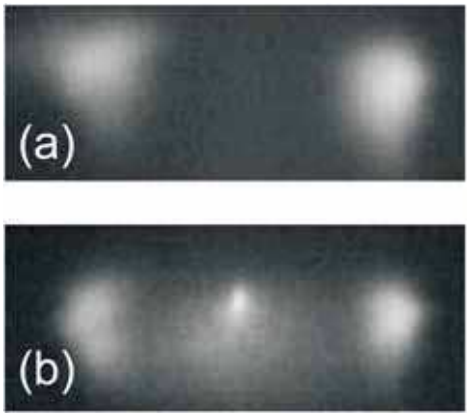

Fig. 3. The typical images of oscillating atomic clouds. The modulation frequency is 75 Hz for (a) and 95 Hz for (b).

The experimental results for the dependence of the amplitude and phase of limit cycles on the modulation frequency [amplitude] are presented in Fig. 5(a) and Fig. 5(b) [Fig. 5(c) and Fig. 5(d)], respectively. In Figs. 5(a) and (b), h = 0.7 and 0.9. Figs. 5(a) and (b), the solid [dotted] lines and curves are calculated results from the Eq. (1) while the filled squares [hollow circles] denote the experimental results at the modulation amplitude of h=0.9 [0.7]. In Figs. 5(c) and (d), the modulation frequency is $\omega = 2\pi \times$ 65 Hz. The threshold amplitude (h_T) is 0.40, but we need at least h = 0.6 to observe the parametric resonance. In Fig. 5, we can clearly see the good agreement between the experiments and the calculations.

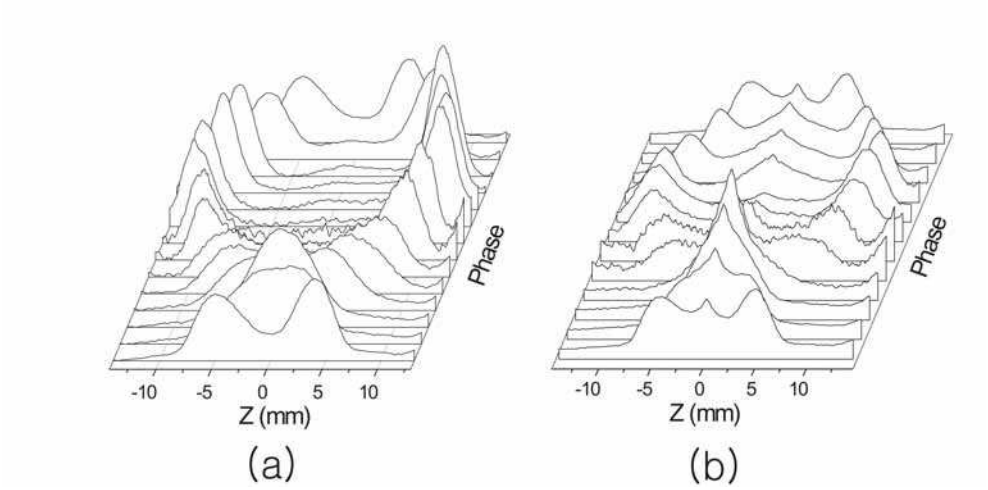

Fig. 4. Profiles of the oscillating clouds at the various phases with respect to the modulations at the frequency of Region I (a) and Region II (b).

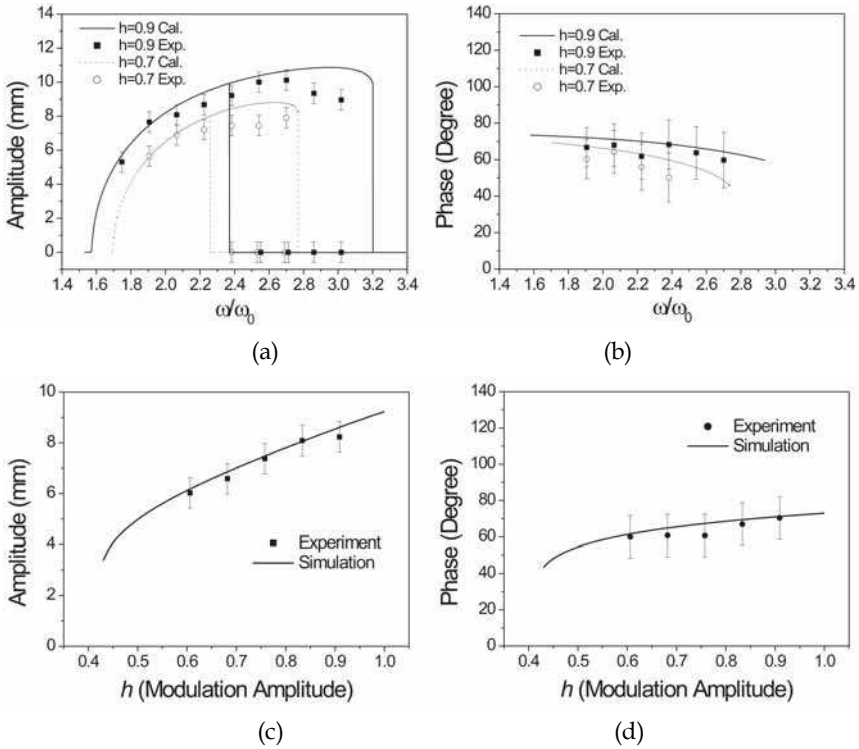

Fig. 5. The dependence of amplitude (a) [(c)] and phase (b) [(d)] of limit cycles on the modulation frequency [amplitude].

2.3 Observation of sub-Doppler trap

In this subsection we describe the direct observation of sub-Doppler part of the MOT through the parametric resonance (Kim et al., 2004). Typical experimental parameters are as follows: in the z-axis, $s_0 = 0.05$, $b = 9$ G/cm, the amplitude of modulation $h = 0.9$, and $\delta/\Gamma = -2.9$. Thus ω_{dop} is about $2\pi\times$ 34.3 Hz, and ω_{sub} (will be explained later) is $2\pi\times$ 460 Hz. The full width of MOT beams at the $e^{-1/2}$ intensity point is 2.5 cm in order to cover the whole range of atomic motion ($2R$). The total number of atoms in the unmodulated MOT is about 2×10^8 and that in the modulated MOT is about 8×10^7. Figure 6 shows the photos of parametrically excited atoms at the modulation frequency of 80 Hz (a) and 95 Hz (b). Both frequencies belong to region I and II in Fig. 1(c), respectively. We can easily notice that the broad and large trap in Fig. 6(b) is attributable to the third fixed point at the origin of the magnetic field with the Doppler theory. On the other hand, the narrow and sharp traps in Fig. 6(a) and (b) have a different origin, which can be very well understood by including the sub-Doppler cooling theory (Chang & Minogin, 2002; Jun et al, 1999).

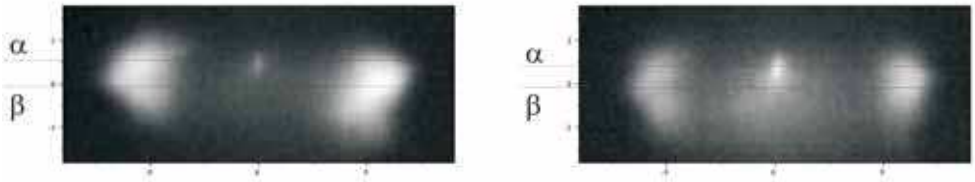

(a) (b)

Fig. 6. The typical appearance of (a) double and (b) triple fixed points in experiments. The modulation frequency is 80 Hz (a) and 95 Hz (b).

There exist two kinds of trap in a normal MOT: One is due to one photon process, that is, Doppler cooling theory, and the other is due to two photon process, which makes sub-Doppler temperature (Jun et al, 1999). Thus the force exerted on an atom is given by

$$F(z,v,t) = F_{\mathrm{dop}}(z,v,t) + F_{\mathrm{sub}}(z,v,t), \tag{13}$$

where the Doppler force ($F_{\mathrm{dop}}(z,v,t)$) is given in Eq. (2) and the sub-Doppler force for a $F = 1 \rightarrow F' = 2$ atomic transition line is analytically given by (Jun et al, 1999)

$$F_{\mathrm{sub}}(z,v,t) = f\left(\frac{kv}{\Gamma} + \frac{g_g \mu_B b z}{\hbar\Gamma}\right). \tag{14}$$

Here the function $f(x)$ is given by

$$f(x) = -\frac{120\hbar k\Gamma s(t)^2 \,|\, \delta/\Gamma \,|\, x}{17s(t)^2\left[5 + 4(\delta/\Gamma)^2\right] + 2112\left[1 + 4(\delta/\Gamma)^2\right]^2 x^2},$$

with g_g the g–factor of the ground state and $s(t) = s_0(1 + h\cos\omega t)$. Fig. 7(a) shows the typical calculation of the total force and Fig. 7(b) shows the same force for the detailed region for $F = 1 \rightarrow F' = 2$ atomic transition line. We can see that the sub-Doppler force exists only near the origin. Although the sub-Doppler force for other transition lines can be calculated numerically (Walhout et al., 1992), we used Eq. (14) for the sub-Doppler force the transition $F = 3 \rightarrow F' = 4$ of ^{85}Rb atoms with $g_g = 1/3$. The trap frequency can be derived from Eq. (14) as

$$\omega_{sub} = \sqrt{\frac{P_1 \mu_B b k \,|\, \delta / \Gamma \,|}{m\left[1 + P_2 (\delta / \Gamma)^2\right]}} \,. \tag{15}$$

with the coefficients $P_1 = 24/17$ and $P_2 = 4/5$ for 1→2, $P_1 = 6.84$ and $P_2 = 2.72$ for 2→3, and $P_1 = 12.5$ and $P_2 = 3.57$ for 3→4 transition line.

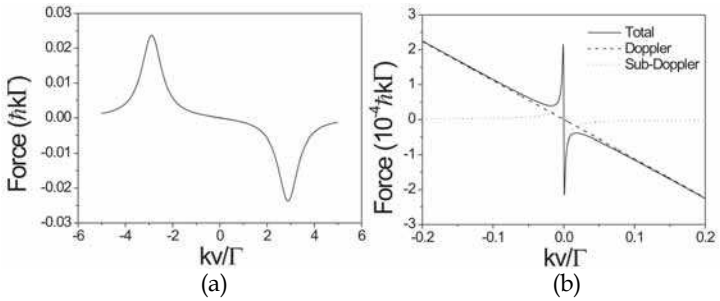

Fig. 7. The calculated total force in the enlarged (a) and detailed region (b).

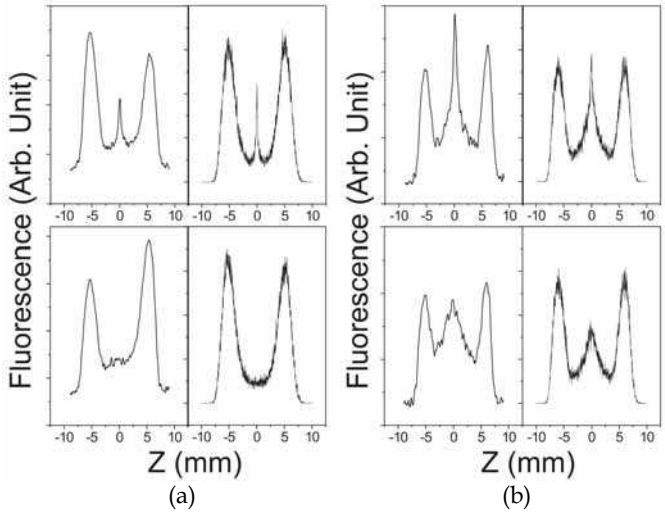

Fig. 8. Upper and Lower panels of (a)[(b)] is the profile of Fig. 6(a)[(b)] along α and β-line, respectively. In each panel, the left one is the measured profile and the right one is the simulation result.

The profiles of Fig. 6 are compared to the Monte-Calro simulations with and without considering the sub-Doppler force. Upper [Lower] panel of Figure 8(a) and 8(b) is the profile of Fig. 6(a) and 6(b), respectively along the α [β]-line. In the figures the left one is the experimental data and the right one is the simulation result. In Fig. 8(a), the experimental (simulation) result of width (twice the standard deviation in the Gaussian distribution) of broad peaks is approximately 2.1 mm (2.2 mm). Also the experimental (simulation) width of central peak is 0.45 mm (0.28 mm). In Fig 8(b), the experimental (simulation) width of oscillating broad peak, central broad peak, and the central sharp peak is 1.7 (1.9) mm, 5.6

(5.2) mm, and 0.68 (0.26) mm, respectively. We can see the good agreements between the experimental and simulation results. We used the combined force (Eq.(13)) in the simulation. In addition, we also take into account the random recoil force, f_r, from the spontaneously emitted photons. The random force is related with the momentum diffusion via the following equation:

$$< f_r(t) f_r(t') >= 2D_{zz}(t)\delta(t-t') , \tag{16}$$

where $D_{zz}(t)$ is the momentum diffusion coefficient for z-axis and the left-hand side of Eq. (16) denotes the average of product of the force at the different time over long time. The momentum diffusion coefficients for various transition lines are presented in Fig. 9(a) (Walhout et al., 1992), where we have assumed the unmodulated laser intensity, i.e., $s(t) = s_0$. In Fig. 9(a) the result for $F = 0 \rightarrow F' = 1$ corresponds to that of Doppler theory. The calculated results for the detailed region are shown in Fig. 9(b). Near the center of the velocity, there exists a sharp dip, which exhibits the feature of two-photon resonance, that is, sub-Doppler laser cooling theory. In the simulation we have used the calculated momentum diffusion coefficient in the sub-Doppler cooling theory for $F = 3 \rightarrow F' = 4$ transition line.

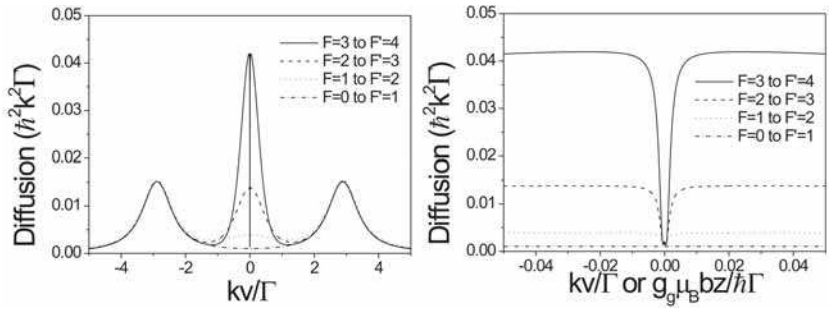

(a) (b)

Fig. 9. (a) The calculated momentum diffusion coefficients for various atomic transition lines. (b) The detailed plots near the origin.

3. Measurement of trap parameters

3.1 Parametric resonance method

Since the spring constant is one of the basic parameters of a MOT, there has been much effort to measure the spring constant, inferred from the measured spatial profile and the temperature by means of the equi-partition theorem (Drewsen et al., 1994; Wallace et al., 1994), by using the beam imbalance (Wallace et al., 1994; Steane et al., 1992) or by using the imposed oscillating magnetic field (Kohns et al., 1993; Hope et al., 1993). Authors in Ref. (Xu et al., 2002) have used the method of free oscillation of atoms after rapid turning-off the constant pushing laser beam and study the three-dimensional Doppler cooling theory for two-level atoms. In Sec. 3, we present two methods to measure the trap parameters of the MOT such as the trap frequency and the damping coefficient. The first method, described in this subsection, is based on the parametric resonance described in the preceding section (Kim et al., 2005). The second is the method of transient oscillation of atomic trajectory (Kim et al., 2005), which is presented in the next subsection.

With a larger modulation amplitude, the parametric resonance occurs at a wider range of the modulation frequency. However, when the modulation amplitude decreases towards its threshold value, the amplitude becomes a Gaussian-like shaped function centered at twice the natural frequency. Therefore, one can accurately measure the trap frequency and thus the spring constant as well. In the experiment, the laser intensity in the z-axis was I_z = 0.099 mW/cm^2, while the intensities along the transverse directions were $I_x = I_y = 5I_z$. The modulation amplitude is decreased down to h = 0.5 to observe the trap frequency accurately. The full width of laser beams at the $e^{-1/2}$ intensity point is 2.5 cm to cover the whole atomic motion. When atoms are parametrically excited, the number of atoms decreases to about 8 $\times 10^7$. The laser detuning is about $\Delta = -2.3\Gamma$, where $\Gamma = 2\pi \times$ 5.9 MHz is the decay rate of the excited state. In the experiment we vary the magnetic field gradient to study the dependence of the spring constant on the magnetic field gradient.

By varying the modulation amplitude, we measure the amplitudes of limit cycle motions as presented in Fig. 10(a). When h is large, two oscillating clouds with the phase difference of π can be clearly seen. As h decreases, two peaks approach each other and merge into a single cloud. In Fig. 10(a), the modulation frequency is f = 84 Hz. Figure 10(b) shows the typical experimental results for three values of the magnetic field gradients (b). For a given b, we vary the modulation frequency (f) and measure the width of single-merged cloud. Varying f, the amplitude has a peak at a certain frequency, which is approximately given by $f = 2f_0$.

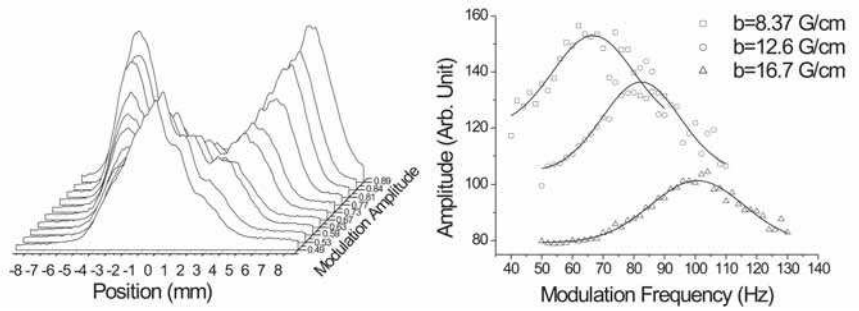

(a) (b)

Fig. 10. (a) The measured profiles of limit cycle motions at the various modulation amplitudes h (f = 84 Hz). (b) The measured profiles as functions of the modulation frequency for three magnetic filed gradients.

The measured trap frequencies (filled squares) for several magnetic field gradients are shown in Fig. 11(a). The curves in Fig. 11(a) are the theoretical results. The curves A and C are the results calculated by Eq. (4a) with the normalized saturation intensities $s_0 = I_z/I_s$ and $s_0 = I_z/(I_s)_{av}$, respectively. Here $(I_s)_{av}$ = 3.78 mW/cm^2 is the averaged saturation intensity (Wallace et al., 1994). With the averaged saturation intensity, the result agrees well with experimental results. The curves B and D are the calculated results based on the rate equation model for $F_g = 0 \rightarrow F_e = 1$ and $F_g = 3 \rightarrow F_e = 4$ transition lines, respectively. We can see that the results of line C and D are almost equal and agree with the experimental results. The details of calculation using the rate equation model are presented in Ref. (Kim et al., 2005). The results for κ/b for the varying the intensities of $I_x + I_y$ are shown in Fig. 11(b), where $\kappa = m\omega_0^2$ is the spring constant. Since the spring constant is proportional to the

magnetic field gradient (b), we have a constant value for all experimental data. As the laser intensity for the transverse directions increases, κ_0/b decreases. In Fig. 11(b), we find that the use of the averaged saturation intensity ($(I_s)_{av}$) is a good approximation at the broad range of the transverse laser intensities.

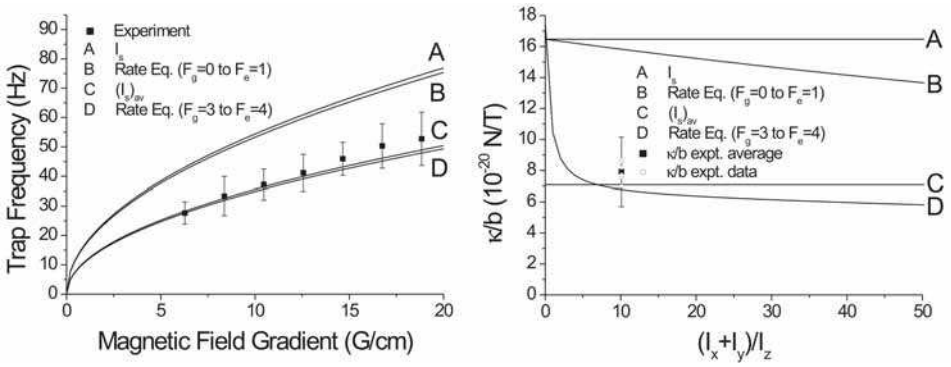

(a) (b)

Fig. 11. (a) The measured trap frequencies versus the the magnetic field gradients (filled squares). (b) The spring constants divided by the magnetic filed gradient.

3.2 Transient oscillation method

In this subsection, we present measurement of the trap frequency as well as the damping coefficient by detecting the temporal oscillatory behavior of the pushed atomic cloud as the magnetic field gradient or the laser detuning is varied (Kim et al., 2005). The atomic motion in the MOT is simply given by a damped harmonic oscillator model with the damping coefficient β and the trap frequency f_0. When a uniform magnetic field (B_z) is applied to the MOT, the position of the trap center is shifted by B_z/b, where b is the magnetic field gradient in the z-axis of the MOT. When the uniform magnetic field is suddenly turned off, the atomic cloud returns to the original trap center. In case of the underdamped motion, one can extract the trap parameters by measuring the trajectory of the released atomic cloud. The trajectory of the atomic cloud center is simply given by

$$z(t) = z_0 + A\exp(-\beta t/2)\left(\cos 2\pi f_0 t + \frac{\beta}{4\pi f_0}\sin 2\pi f_0 t\right), \tag{17}$$

where $f_0 = \omega_0/(2\pi)$ is the trap frequency, β is the damping coefficient, z_0 is the equilibrium position, and A is the initial displacement from equilibrium.

Figure 12(a) shows the contour-plot of the typical absorption signals of the 16-channel photodiode array versus time (taken at 1/5000 s time interval), superposed by a curve corresponding to the maximum brightness. Here the vertical axis shows the position of the photodiode array and horizontal axis represents the time elapsed after switch off of the magnetic field. Figure 12(b) shows the same curve as in Fig. 12(a) and its fitted result using Eq. (17) for the region after elapse of one period, which is shown in the lower panel. From the fit presented in Fig. 12(b) one can obtain the trap frequency and the damping coefficient.

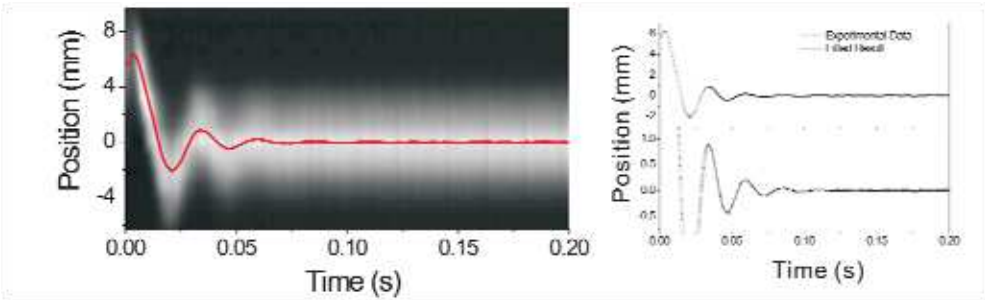

(a) (b)

Fig. 12. (a) The contour plot of the signals showing a typical oscillating motion of atomic cloud. (b) The same curve as in (a) and the fitted curve obtained by Eq. (17). The detailed plot after one period is shown in the lower panel.

We have measured the trap parameters by varying the laser intensity, detuning, and magnetic field gradient. The results are presented in Figs. 13. Fig. 13 shows the dependence of trap frequency (a)[(c)] and damping coefficient (b)[(d)] on the magnetic field gradient [detuning]. In Figs. 13(a) and (b), $\Delta = -2.71\Gamma$, and I_z = 0.10 mW/cm² (filled square), 0.13 mW/cm² (filled circle) and 0.17 mW/cm² (filled triangle), respectively. Note that the laser intensities in the transverse directions ($I_x = I_y$) are 0.62 mW/cm². The solid, dashed, and dashed-dotted lines in the figure are the calculated results from a theoretical model. In Figs. 13(c) and (d), I_z = 0.17 mW/cm², $I_x = I_y$ = 0.62 mW/cm², and b = 10 G/cm. Note that the solid line is obtained from the rate equation for the Doppler theory, whereas the dashed line is from the simple Doppler theory for two level atom where the saturation intensity is

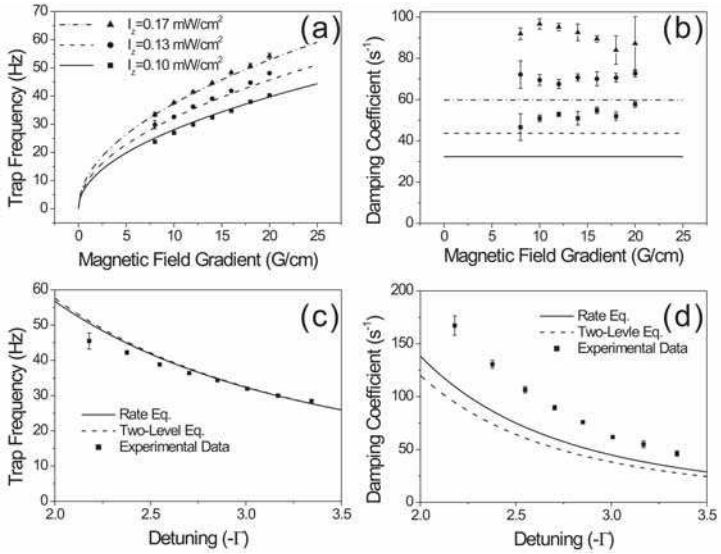

Fig. 13. The dependence of the trap frequency (a)[(c)] and damping coefficient (b)[(d)] on the magnetic field gradient [detuning].

substituted by the averaged value $(I_s)_{av}$ = 3.78 mW/cm^2. As shown in Fig. 13, the trap frequencies are in good agreement with the theoretical values. The damping coefficients, on the other hand, are about twice larger than the simple theoretical predictions. We provide a quantitative description of the theoretical model and explain the discrepancy found in the damping coefficient.

The summary of the data of Fig. 13 is presened in Fig. 14. The damping coefficient and the trap frequency are presented as a function of $s_0\delta/(1+4\delta^2)^2$ and $\sqrt{bs_0\delta}\,/(1+4\delta^2)$, respectively.

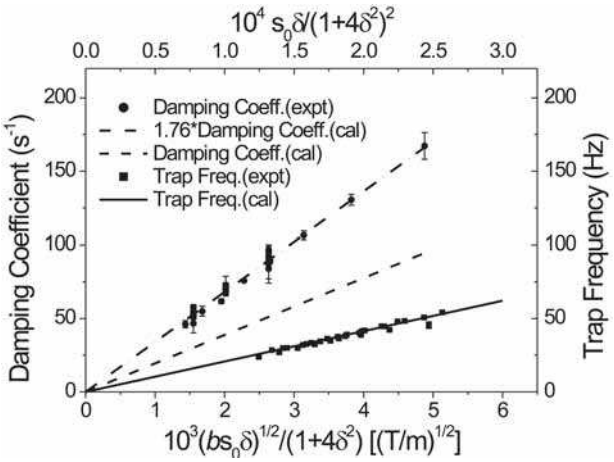

Fig. 14. The damping coefficient versus $s_0\delta/(1+4\delta^2)^2$ [filled circles, experimental data; dashed line, calculated results; dashed-dotted line, calculated results multiplied by 1.76] and the trap frequency versus $\sqrt{bs_0\delta}\,/(1+4\delta^2)$ [filled squares, experimental data; solid line, calculated results].

One can observe that the measured trap frequencies are in excellence agreement with the calculated results. On the other hand, one has to multiply the simply calculated damping coefficients by a factor 1.76 to fit the experimental data. We find that the discrepancy in the damping coefficients results from the existence of the sub-Doppler trap described in Sec. 2.3. In order to show that the existence of the sub-Doppler force affects the Doppler-cooling parameters, we have performed Monte-Carlo simulation with 1000 atoms. In the simulation, we used sub-Doppler forces and momentum diffusions described in Sec. 2.3. The results are presented in Fig. 15. Here we averaged the trajectories for 1000 atoms by using the same parameters as used in Fig. 12. We have varied the intensity (I) associated with F_{sub} without affecting the intensity for the Doppler force, and obtained the averaged trajectory, where I_{expt} =0.17 mW/cm^2 is the laser intensity used in the experiment [Fig. 13]. We then infer the damping coefficient and the trap frequency by fitting the averaged trajectory with Eq. (17). The fitted results for the damping coefficient and the trap frequency are shown in Fig. 15(b). While the trap frequency remains nearly constant, the damping coefficient increases with the intensity. Note that to obtain an increase of factor 1.76 as shown in Fig. 14, one should use I/I_{expt} = 1.6. The reason for the increase of the damping coefficient can be well explained qualitatively from the simulation.

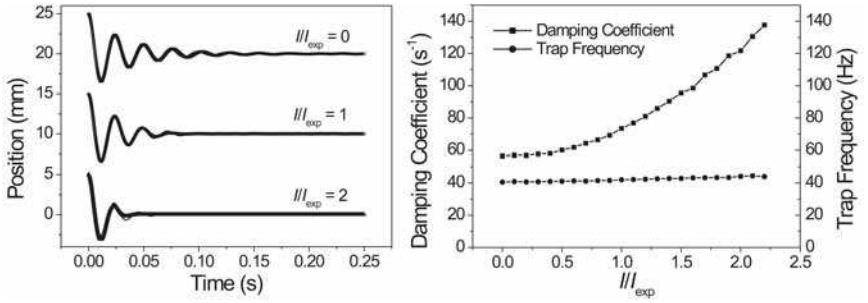

(a) (b)

Fig. 15. The Monte-Carlo simulation results. (a) The averaged trajectories for 1000 atoms together with the fitted curves obtained from Eq. (17). (b) The damping coefficient (filled square) and the trap frequency (filled circle) as a function of the laser intensity.

4. Adjustable magneto-optical trap

When the detuning and intensity of the longitudinal (z-axis) lasers along the symmetry axis of the anti-Helmholtz coil of the MOT are different from those of the transverse (x and y axis) lasers, one can realize an array of several sub-Doppler traps (SDTs) with adjustable separations between traps (Heo et al., 2007; Noh & Jhe, 2007). As shown in Fig. 16(a), it is similar to the conventional six-beam MOT, except that the detunings (δ_x and δ_y) and intensities (I_x and I_y) of the transverse lasers can be different from those of the longitudinal ones (δ_z and I_z). In the case of usual MOT, one obtains a usual Doppler trap superimposed with a tightly confined SDT at the MOT center, exhibiting bimodal velocity as well as spatial distributions (Dalibard, 1988; Townsend et al., 1995; Drewsen et al., 1994; Wallace et al., 1994; Kim et al., 2004). Under equal detunings but unequal intensities (I_x, $I_y \gg I_z$), which typically arise in the nonlinear dynamics study of nonadiabatically driven MOT (Kim et al., 2003; 2006), one still obtains the bimodal distribution. However, as the transverse-laser detuning δ_t ($\equiv \delta_x = \delta_y$) is different from the longitudinal one δ_z with the same configuration of laser intensity, the SDT at the center becomes suppressed with the usual Doppler trap still present. The existence of the central SDT, available at equal detunings, contributes not only to the lower atomic temperature but also to the larger damping coefficients than is expected

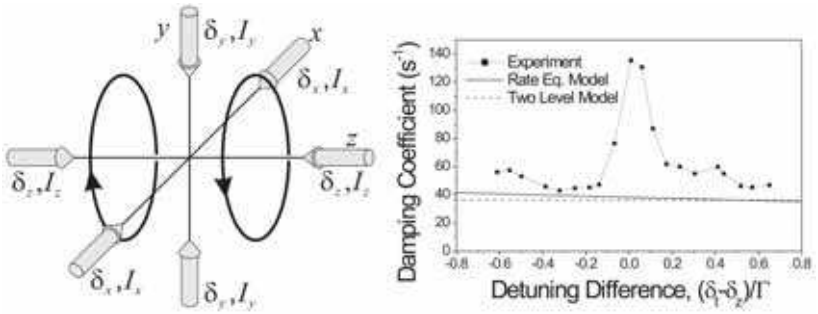

(a) (b)

Fig. 16. (a) Schematic of the asymmetric magneto-optical trap. (b) Measured damping coefficients versus normalized laser-detuning differences.

by the Doppler theory. In order to confirm the enhanced damping, we have measured the damping coefficients of MOT versus the laser detuning differences, $\delta_t - \delta_z$, by using the transient oscillation method described in Sec. 3.2 (Kim et al., 2005). As is shown in Fig. 16(b), one can observe a 'resonance' behaviour; the damping coefficient is suppressed by more than a factor of 2 and approaches the usual Doppler value at unequal detunings, which is directly associated with the disappearance of the central SDT.

When the transverse laser intensity is increased above a certain value at unequal detunings, we now observe the appearance of novel SDTs. In Fig. 17, the fluorescence images of the trapped atoms, obtained with $I_t \equiv I_x + I_y = 11.4I_z$ fixed, are presented for various values of $\delta_t - \delta_z$. The central peak, corresponding to the usual SDT, becomes weak when the detunings are different, as discussed in Fig. 16(b). However, the two side peaks, associated with the novel SDTs, are displaced symmetrically with respect to the MOT center, in proportion to $\delta_t - \delta_z$. In addition to these two adjustable side SDTs, there also exist another two weak SDTs located midway between each side SDT and the central one, which will be discussed later.

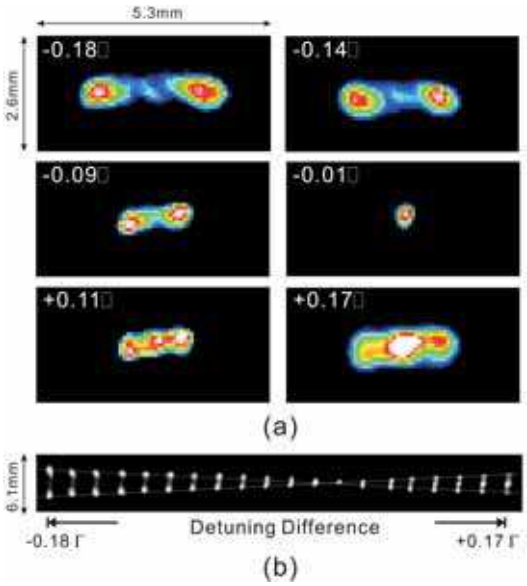

Fig. 17. (a) Fluorescence images that show two adjustable side SDTs for several values of $\delta_t - \delta_z$. (b) SDT pictures plotted in series with the increasing detuning differences.

In Fig. 18(a), we plot the positions of the two side SDTs for various values of $\delta_t - \delta_z$, represented by filled squares, which are also shown in Fig. 17(b). Attributed to the coherences between the ground-state magnetic sublevels with $\Delta m = \pm 1$ transitions (see Fig. 18(b)), the two side SDTs appear at the positions $z_S = \pm\hbar(\delta_t - \delta_z)/(g_g \mu_B b)$ and thus their separation satisfies,

$$\frac{\Delta z_S}{\Delta \nu} = \pm \frac{h}{\mu_B b g_g}, \tag{18}$$

where $\Delta\nu = (\delta_t - \delta_z)/(2\pi)$ and μ_B is the Bohr magneton. Since the ground-state g-factor is $g_g = 1/3$ for ^{85}Rb atoms and the magnetic field gradient is $b = 0.17$ T/m, the calculated value

(solid line) is $\Delta z/\Delta\nu$ = 1.26 mm/MHz, which agrees well with the experimental result of 1.25 (±0.12) mm/MHz, considering 10% error of position measurements. On the other hand, the two weak SDTs, resulting from the coherences due to Δm = ±2 transitions (refer to Fig. 18(b)), are located midway at $z_M = z_S/2$, as shown in Fig. 18(a) (open circles). The fitted result is 0.61 mm/MHz, which is almost half the value given by Eq. (18), in good agreement with the 'doubled' energy differences of the Δm = ±2 transitions with respect to the Δm = ±1 ones, responsible for the side SDTs.

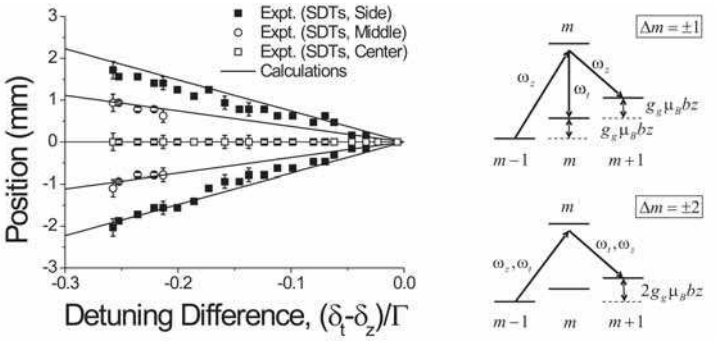

(a) (b)

Fig. 18. Measured positions of available SDTs versus negative detuning differences.

In order to have a qualitative understanding of the detuning-difference dependence, we have calculated the cooling and trapping forces in two dimension by using the optical Bloch equation approach (Dalibard, 1988; Chang & Minogin, 2002; Noh & Jhe, 2007). In Fig. 19(a), we present the calculated forces $F(z,v = 0)$ for $F_g = 3 \rightarrow F_e = 4$ atomic transition. In the presence of the transverse lasers, the ground-state sublevels with Δm = ±1 transitions can be coupled by a π photon from the transverse lasers in combination with a $\sigma^{\pm}$ photon from the longitudinal lasers (see Fig. 18(b)). As a result, for unequal detunings, there exists a position where the Zeeman shift compensates the laser-frequency difference, such that

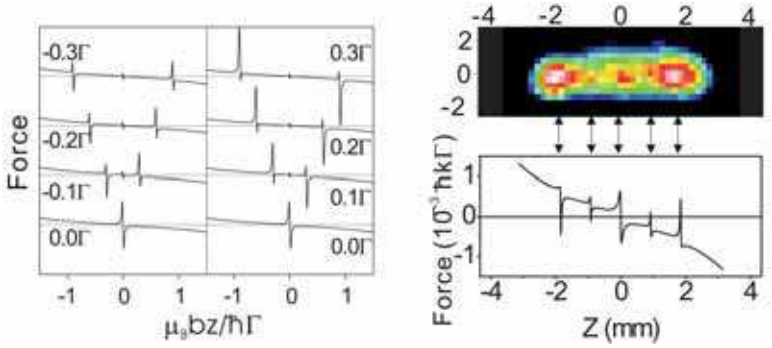

(a) (b)

Fig. 19. (a) Calculated forces $F(z,v = 0)$ for various detuning differences. The maximum forces at 0.3 Γ corresponds to 5×10^{-3} $\hbar k\Gamma$. Here $\delta_z = -2.7\Gamma$, $I_z = 0.11$ mW/cm², and $I_t = 5.6I_z$. (b) Five SDTs, including two weak SDTs midway between the two side SDTs and the central one, for $\delta_t - \delta_z = -0.24\Gamma$.

$$\hbar\omega_z - \hbar\omega_t = \pm g_g \mu_B b z. \tag{19}$$

At this position, atoms can feel the sub-Doppler forces associated with the $\Delta m = \pm 1$ coherences and thus the novel SDT is obtained at two positions of $\pm\hbar(\delta_x - \delta_z)/(g_g\mu_B b)$, as confirmed in Fig. 18(a). As shown in Fig. 19(b), the two weak midway SDTs arise because the weak $\sigma^{\pm}$ photons, in addition to the dominant π ones, from the transverse lasers can contribute to the atomic coherences in the z-direction. Therefore, besides the $\Delta m = \pm 1$ transitions responsible for the side SDTs, the two-photon-assisted $\Delta m = \pm 2$ coherences (here, each $\sigma^{\pm}$ photon comes from the longitudinal and the transverse laser, as shown in Fig. 18(b)) can be generated, and atoms at the position z_M, satisfying the relation $\hbar\omega_t - \hbar\omega_z = \pm 2 g_g \mu_B b z_M$, feel this additional coherence. As a result, the midway SDTs can be obtained at $z_M = z_S/2$ (see Fig. 18(a)). The typically observed image and the calculated force are presented in Fig. 19(b).

5. Conclusions

In this article we have presented experimental and theoretical works on the asymmetric magneto-optical trap. In Sec. 2, we have studied parametric resonance in a magneto-optical trap. We have described a theoretical aspect of parametric resonance by the analytic and numerical methods. We also have measured the amplitude and phase of the limit cycle motions by changing the modulation frequency or the amplitude. We find that the results are in good agreement with the calculation results, which are based on simple Doppler cooling theory. In the final subsection we described direct observation of the sub-Doppler part of the MOT without the Doppler part by using the parametric resonance which. We compared the spatial profile of sub-Doppler trap with the Monte-Carlo simulation, and observed they are in good agreements.

In Sec. 3, we have presented two methods to measure the trap frequency: one is using parametric resonance and the other transient oscillation method. In the case of parametric resonance method, we could measure the trap frequency accurately by decreasing the modulation amplitude of the parametric excitation down to its threshold value. While only the trap frequency were able to be obtained by the parametric resonance method, we could obtain both the trap frequency and the damping coefficient by the transient oscillation method. We have made a quantitative study of the Doppler cooling theory in the MOT by measuring the trap parameters. We have found that the simple rate-equation model can accurately describe the experimental data of trap frequencies.

In Sec. 4, we have demonstrated the adjustable multiple traps in the MOT. When the laser detunings are different, the usual sub-Doppler force and the corresponding damping coefficient at the MOT center is greatly suppressed, whereas the novel sub-Doppler traps are generated and exist within a finite range of detuning differences. We have found that π and $\sigma^{\pm}$atomic transitions excited by the transverse lasers in the longitudinal direction are responsible for the strong side and the weak middle sub-Doppler traps, respectively. The adjustable array of sub-Doppler traps may be useful for controllable atom-interferometer-type experiments in atom optics or quantum optics.

The AMOT described in this article can be used for study of nonlinear dynamics using cold atoms such as critical phenomena far from equilibrium (Kim et al., 2006) or a nonlinear Duffing oscillation (Nayfeh & Moore, 1979; Strogatz, 2001).

6. Acknowledgement

This work was supported by the Korea Research Foundation Grant funded by the Korean Government (KRF-2008-313-C00355).

7. References

Bagnato, V. S., Marcassa, L. G., Oria, M., Surdutovich, G. I., Vitlina, R. & Zilio, S. C. (1993). Spatial distribution of atoms in a magneto-optical trap, *Phys. Rev. A* Vol. 48(No. 5): 3771–3775.

Chang, S. & Minogin, V. (2002). Density-matrix approach to dynamics of multilevel atoms in laser fields, *Phys. Rep.* Vol. 365(No. 2): 65–143.

Dalibard, J. (1998). Laser cooling of an optically thick gas: The simplest radiation pressure trap?, *Opt. Commun.* Vol. 68(No. 3): 203–208.

di Stefano, A., Fauquembergue, M., Verkerk, P. & Hennequin, D. (2003). Giant oscillations in a magneto-optical trap, *Phys. Rev. A* Vol. 67(No. 3): 033404-1–033404-4.

Dias Nunes, F., Silva, J. F., Zilio, S. C. & Bagnato, V. S. (1996). Influence of laser fluctuations and spontaneous emission on the ring-shaped atomic distribution in a magneto-optical trap, *Phys. Rev. A* Vol. 54(No. 3): 2271–2274.

Drewsen, M., Laurent, Ph., Nadir, A., Santarelli, G., Clairon, A., Castin, Y., Grinson, D. & Salomon, C. (1994). Investigation of sub-Doppler cooling effects in a cesium magnetooptical trap, *Appl. Phys. B* Vol. 59(No. 3): 283–298.

Friebel, S., D'Andrea, C., Walz, J., Weitz, M. & H¨ansch, T. W. (1998). CO_2-laser optical lattice with cold rubidium atoms, *Phys. Rev. A* Vol. 57(No. 1): R20–R23.

Heo, M. S., Kim, K., Lee, K. H., Yum, D., Shin, S., Kim, Y., Noh, H. R. & Jhe, W. (2007). Adjustable multiple sub-Doppler traps in an asymmetric magneto-optical trap, *Phys. Rev. A* Vol. 75(No. 2): 023409-1–023409-4.

Hope, A., Haubrich, D., Muller, G., Kaenders, W. G. & Meschede, D. (1993). Neutral cesium atoms in strong magnetic-quadrupole fields at sub-doppler temperatures, *Europhys. Lett.* Vol. 22(No. 9): 669–674.

Jun, J. W., Chang, S., Kwon, T. Y., Lee, H. S. & Minogin, V. G. (1999). Kinetic theory of the magneto-optical trap for multilevel atoms, *Phys. Rev. A* Vol. 60(No. 5): 3960–3972.

Kim, K., Noh, H. R., Yeon, Y. H. & Jhe,W. (2003). Observation of the Hopf bifurcation in parametrically driven trapped atoms, *Phys. Rev. A* Vol. 68(No. 3): 031403(R)-1–031403(R)-4.

Kim, K., Noh, H. R. & Jhe, W. (2004). Parametric resonance in an intensity-modulated magneto-optical trap, *Opt. Commun.* Vol. 236(No. 4-6): 349–361.

Kim, K., Noh, H. R., Ha, H. J. & Jhe, W. (2004). Direct observation of the sub-Doppler trap in a parametrically driven magneto-optical trap, *Phys. Rev. A* Vol. 69(No. 3): 033406-1–033406-5.

Kim, K., Noh, H. R. & Jhe, W. (2005). Measurements of trap parameters of a magneto-optical trap by parametric resonance, *Phys. Rev. A* Vol. 71(No. 3): 033413-1–033413-5.

Kim, K., Lee, K. H., Heo, M., Noh, H. R. & Jhe, W. (2005). Measurement of the trap properties of a magneto-optical trap by a transient oscillation method, *Phys. Rev. A* Vol. 71(No. 5): 053406-1–053406-5.

Kim, K., Heo, M. S., Lee, K. H., Jang, K., Noh, H. R., Kim, D. & Jhe, W. (2006). Spontaneous Symmetry Breaking of Population in a Nonadiabatically Driven Atomic Trap: An Ising-Class Phase Transition, *Phys. Rev. Lett.* Vol. 96(No. 15): 150601-1–150601-4.

Kohns, P., Buch, P., Suptitz, W., Csambal, C. & Ertmer, W. (1993). On-Line Measurement of Sub-Doppler Temperatures in a Rb Magneto-optical Trap-by-Trap Centre Oscillations, *Europhys. Lett.* Vol. 22(No. 7): 517–522.

Kulin, S., Killian, T. C., Bergeson, S. D. & Rolston, S. L. (2000). Plasma Oscillations and Expansion of an Ultracold Neutral Plasma, *Phys. Rev. Lett.* Vol. 85(No. 2): 318–321.

Labeyrie, G., Michaud, F. & Kaiser, R. (2006). Self-Sustained Oscillations in a Large Magneto-Optical Trap, *Phys. Rev. Lett.* Vol. 96(No. 2): 023003-1–023003-4.

Landau, L. D. & Lifshitz, E. M. (1976). *Mechanics*, Pergamon, London.

Lapidus, L. J., Enzer, D. & Gabrielse, G. (1999). Stochastic Phase Switching of a Parametrically Driven Electron in a Penning Trap, *Phys. Rev. Lett.* Vol. 83(No. 5): 899–902.

Metcalf, H. J. & van der Straten, P. (1999). *Laser Cooling and Trapping*, Springer, New York.

Nayfeh, N. H. & Moore, D. T. (1979). *Nonlinear Oscillations*, Wiley, New York.

Noh, H. R. & Jhe, W. (2007). Semiclassical theory of sub-Doppler forces in an asymmetric magneto-optical trap with unequal laser detunings, *Phys. Rev. A* Vol. 75(No. 5): 053411-1–053411-9.

Raab, E. L., Prentiss, M., Cable, A., Chu, S. & Pritchard, D. E. (1987). Trapping of Neutral Sodium Atoms with Radiation Pressure, *Phys. Rev. Lett.* Vol. 59(No. 23): 2631–2634.

Razvi, M. A. N., Chu, X. Z., Alheit, R., Werth, G. & Blümel, R. (1998). Fractional frequency collective parametric resonances of an ion cloud in a Paul trap, *Phys. Rev. A* Vol. 58(No. 1): R34–R37.

Sesko, D., Walker, T. & Wieman, C. (1991). Behavior of neutral atoms in a spontaneous force trap, *J Opt. Soc. Am. B* Vol. 8(No. 5): 946–958.

Steane, A. M., Chowdhury, M. & Foot, C. J. (1992). Radiation force in the magneto-optical trap, *J Opt. Soc. Am. B* Vol. 9(No. 12): 2142–2158.

Strogatz, S. H. (2001). *Nonlinear Dynamics and Chaos*, Perseus, New York.

Tabosa, J. W. R., Chen, G., Hu, Z., Lee, R. B. & Kimble, H. J. (1991). Nonlinear spectroscopy of cold atoms in a spontaneous-force optical trap, *Phys. Rev. Lett.* Vol. 66(No. 25): 3245–3248.

Tan, J. & Gabrielse, G. (1991). Synchronization of parametrically pumped electron oscillators with phase bistability, *Phys. Rev. Lett.* Vol. 67(No. 22): 3090–3093.

Tan, J. & Gabrielse, G. (1993). Parametrically pumped electron oscillators, *Phys. Rev. A* Vol. 48(No. 4): 3105–3121.

Townsend, C. G., Edwards, N. H., Cooper, C. J., Zetie, K. P., Foot, C. J., Steane, A. M., Szriftgiser, P., Perrin, H. & Dalibard. J. (1995). Phase-space density in the magneto-optical trap, *Phys. Rev. A* Vol. 52(No. 2): 1423–1440.

Walhout, M., Dalibard, J., Rolston, S. L. & Phillips, W. D. (1992). σ_+–σ_- Optical molasses in a longitudinal magnetic field, *J Opt. Soc. Am. B* Vol. 9(No. 11): 1997–2007.

Tseng, C. H., Enzer, D., Gabrielse, G. & Walls, F. L. (1999). 1-bit memory using one electron: Parametric oscillations in a Penning trap, *Phys. Rev. A* Vol. 59(No. 3): 2094–2104.

Walker, T., Sesko, D. & Wieman, C. (1990). Collective behavior of optically trapped neutral atomstitle, *Phys. Rev. Lett.* Vol. 64(No. 4): 408–411.

Walker, T. & Feng, P. (1994). Measurements of Collisions Between Laser-Cooled Atoms, *Adv. At. Mol. Opt. Phys.* Vol. 34: 125–170.

Wallace, C. D., Dinneen, T. P., Tan, K. Y. N., Kumarakrishnan, A., Gould, P. L. & Javanainen, J. (1994). Measurements of temperature and spring constant in a magneto-optical trap, *J Opt. Soc. Am. B* Vol. 11(No. 5): 703–711.

Wilkowski, D., Ringot, J., Hennequin, D. & Garreau, J. C. (2000). Instabilities in a Magnetooptical Trap: Noise-Induced Dynamics in an Atomic System, *Phys. Rev. Lett.* Vol. 85(No. 9): 1839–1842.

Xu, X., Loftus, T. H., Smith, M. J., Hall, J. L., Gallagher, A. & Ye, J. (2002). Dynamics in a two-level atom magneto-optical trap, *Phys. Rev. A* Vol. 66(No. 1): 011401-1–011401-4.

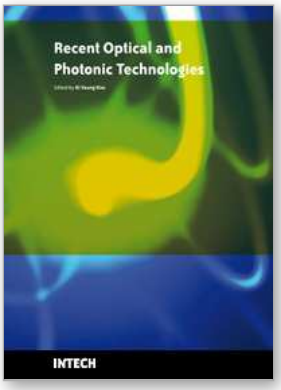

Recent Optical and Photonic Technologies

Edited by Ki Young Kim

ISBN 978-953-7619-71-8
Hard cover, 450 pages
Publisher InTech
Published online 01, January, 2010
Published in print edition January, 2010

Research and development in modern optical and photonic technologies have witnessed quite fast growing advancements in various fundamental and application areas due to availability of novel fabrication and measurement techniques, advanced numerical simulation tools and methods, as well as due to the increasing practical demands. The recent advancements have also been accompanied by the appearance of various interdisciplinary topics. The book attempts to put together state-of-the-art research and development in optical and photonic technologies. It consists of 21 chapters that focus on interesting four topics of photonic crystals (first 5 chapters), THz techniques and applications (next 7 chapters), nanoscale optical techniques and applications (next 5 chapters), and optical trapping and manipulation (last 4 chapters), in which a fundamental theory, numerical simulation techniques, measurement techniques and methods, and various application examples are considered. This book deals with recent and advanced research results and comprehensive reviews on optical and photonic technologies covering the aforementioned topics. I believe that the advanced techniques and research described here may also be applicable to other contemporary research areas in optical and photonic technologies. Thus, I hope the readers will be inspired to start or to improve further their own research and technologies and to expand potential applications. I would like to express my sincere gratitude to all the authors for their outstanding contributions to this book.

INTECH
open science | open minds

InTech Europe
University Campus STeP Ri
Slavka Krautzeka 83/A
51000 Rijeka, Croatia
Phone: +385 (51) 770 447
Fax: +385 (51) 686 166

InTech China
Unit 405, Office Block, Hotel Equatorial Shanghai
No.65, Yan An Road (West), Shanghai, 200040, China
中国上海市延安西路65号上海国际贵都大饭店办公楼405单元
Phone: +86-21-62489820
Fax: +86-21-62489821